Three-dimensional shear wave structure beneath the Philippine Sea from land and ocean bottom broadband seismograms

Takehi Isse,[1] Kazunori Yoshizawa,[2] Hajime Shiobara,[1,3] Masanao Shinohara,[3] Kazuo Nakahigashi,[3] Kimihiro Mochizuki,[3] Hiroko Sugioka,[1] Daisuke Suetsugu,[1] Satoko Oki,[3] Toshihiko Kanazawa,[3] Kiyoshi Suyehiro,[4] and Yoshio Fukao[1]

Received 29 March 2005; revised 16 January 2006; accepted 16 March 2006; published 20 June 2006.

[1] We obtained three-dimensional (3-D) shear wave speed structure beneath the Philippine Sea and the surrounding region from seismograms recorded by land-based and long-term broadband ocean bottom seismographic stations. The ocean bottom data gave us a better station coverage to obtain a higher spatial resolution (about 300–400 km) in the Philippine Sea than in previous studies. We employed a new technique of surface wave tomography, in which multimode phase speeds are measured and inverted for a 3-D shear wave speed structure by incorporating the effects of finite frequency and ray bending. There is a sharp speed contrast along the Izu-Bonin-Mariana trench, across which the Philippine Sea side has a significantly slower upper mantle than the Pacific Ocean side. In the upper 120 km, the shear wave speed structure is well correlated with the age of the provinces. At depths greater than 160 km, the pattern is dominated by fast anomalies of the subducted slabs of the Pacific plate and two slow anomalies to the south of the Daito ridge and in the southernmost part of the Philippine Sea.

Citation: Isse, T., et al. (2006), Three-dimensional shear wave structure beneath the Philippine Sea from land and ocean bottom broadband seismograms, *J. Geophys. Res.*, *111*, B06310, doi:10.1029/2005JB003750.

1. Introduction

[2] The Philippine Sea consists of several small basins, ridges, and troughs with various seafloor ages (Figure 1). This can be explained by a complex history of back-arc spreading of the Philippine Sea plate [e.g., *Hall et al.*, 1995]. The West Philippine Basin, the oldest inactive basin in the Philippine Sea, spread from the Central Basin Fault in ages between 33 and 49 Ma [*Taylor and Goodliffe*, 2004], and the Shikoku and Parece-Vela basins spread between 15 and 27 Ma [*Okino et al.*, 1999]. The Mariana trough is an active back-arc basin and has been spreading since about 6 Ma [*Hussong and Uyeda*, 1981]. The upper mantle structure should reflect this complex evolution history of the Philippine Sea plate.

[3] Since a pioneering work by *Kanamori and Abe* [1968], the upper mantle structure beneath the Philippine Sea has been extensively studied using surface waves mostly under a regionalized approximation [e.g., *Seekins and Teng*, 1977; *Shiono et al.*, 1980; *Oda and Senna*, 1994; *Kato and Jordan*, 1999]. Recently, *Lebedev et al.* [1997] and *Nakamura and Shibutani* [1998] performed regional surface wave tomography to obtain 3-D shear wave speed structure models beneath the Philippine Sea. *Lebedev et al.* [1997] analyzed 281 broadband vertical component seismograms from the Global Seismographic Network and the SKIPPY portable array in Australia by means of waveform inversion with an assumption that surface waves propagate along great circle path. Their model has a higher resolution down to depths of 200–300 km, showing the fast slabs subducted from the Izu-Bonin trench and slow shear wave speed anomaly beneath the Central Basin Fault of the Philippine Sea. *Nakamura and Shibutani* [1998] analyzed Rayleigh waves of 913 event-station pairs to obtain a 3-D shear wave speed structure down to 220 km from the fundamental mode dispersion. Their model is correlated well with the surface tectonics at depths between 80 and 100 km: The uppermost mantle of the older western Philippine Sea is faster than that of the younger eastern Philippine Sea. However, the resolution of the deeper part was limited because they used only the fundamental Rayleigh waves at periods between 30 and 100 s. *Lebedev and Nolet* [2003] obtained a shear wave tomographic model beneath the southeast Asia and western Pacific Ocean including the Philippine Sea by waveform inversion of 4038 vertical component seismograms. Their model shows slow shear wave speeds beneath the Central Basin Fault in good agreement with the previous studies. The model also shows the subducted slab beneath Japan and those beneath the northern Philippine Sea but little slab signatures beneath the Yap and Palau trenches.

[4] In all of these previous models, the lack of seismic stations and earthquakes in the mid Philippine Sea limited

[1]Institute for Research on Earth Evolution, JAMSTEC, Kanagawa, Japan.
[2]Division of Earth and Planetary Sciences, Hokkaido University, Sapporo, Japan.
[3]Earthquake Research Institute, University of Tokyo, Tokyo, Japan.
[4]Independent Administrative Institution, Japan Agency for organization Marine-Earth Science and Technology (JAMSTEC), Kanagawa, Japan.

0148-0227/06/2005JB003750$09.00

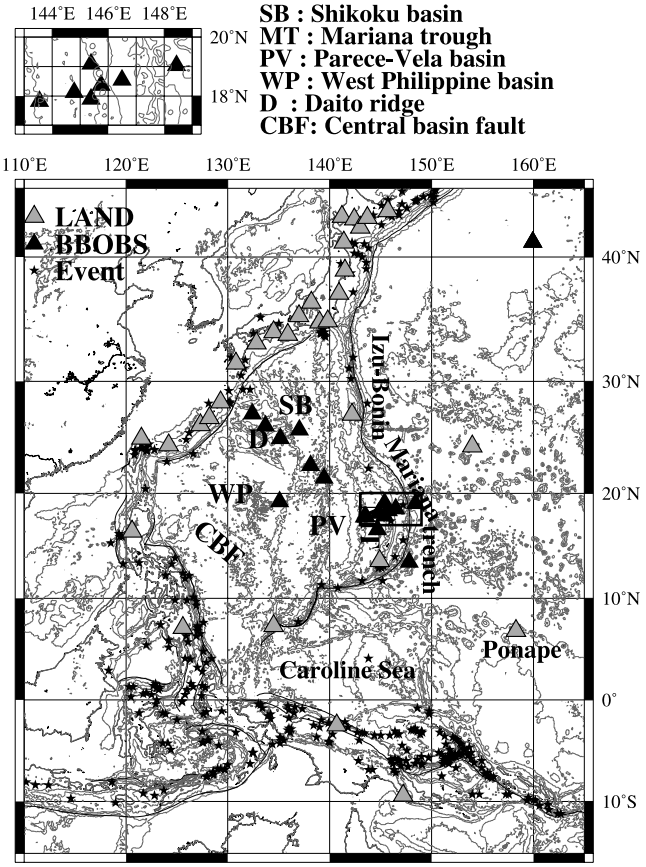

Figure 1. Station and event distributions in the present study. The gray solid triangles are stations on islands, black solid triangles BBOBS stations, and solid stars the event locations. Black square shows the location of a small map at the top. This small map shows the detail of the BBOBS station distribution across the Mariana trough.

the lateral resolution of the shear wave speed structures and made it difficult to eliminate the artifact due to effects of the structure outside the Philippine Sea. The ray theoretical great circle assumption for surface wave propagation, which was used in the previous studies, may not be warranted in such a zone as the rim of the Philippine Sea across which shear wave speed changes sharply.

[5] Since 1990s, the number of stations around the Philippine Sea plate has increased: A dense broadband seismic network F-net (formerly called FREESIA) was deployed across Japan by the National Institute for Earth Science and Disaster Prevention (NIED) [*Fukuyama et al.*, 1996]; A broadband seismic network was established in the western Pacific Ocean by the Ocean Hemisphere network Project (OHP) [*Fukao et al.*, 2001], along which broadband ocean bottom seismometers (called BBOBS hereafter) have also been installed in the Philippine Sea and northwestern Pacific [*Kanazawa et al.*, 2001; *Shiobara et al.*, 2001]. *Isse et al.* [2004] obtained the phase speed maps of the fundamental Rayleigh waves in the northern Philippine Sea by using the seismograms recorded by land-based and ocean bottom broadband stations. It was the first attempt to reveal the mantle structure by using the long-term broadband ocean bottom seismometers. They measured phase speed dispersions by a two-station method and showed that the quality of BBOBS was comparable with that of land stations in the period between 20 and 100 s, indicating that the BBOBS was useful for surface wave studies.

[6] In the present study, we attempt to determine a more accurate 3-D shear wave structure with a higher resolution than in previous studies using Rayleigh waves recorded by land-based and ocean bottom seismic stations. We employ a new inversion technique of surface wave analysis, the three-stage inversion, which makes it possible to incorporate the effects of multimode dispersion, off-great circle propagation, and the finite frequency of Rayleigh wave in a common framework [*Kennett and Yoshizawa*, 2002; *Yoshizawa and Kennett*, 2004]. The use of the multimode phase dispersion data should resolve better the depth variation of shear wave speed than the conventional analysis method of fundamental mode dispersion. Corrections for the off-great circle propagation and finite frequency effects should improve resolution and accuracy of a 3-D model as in the present case where the lateral variation in seismic wave speed is large and sharp.

2. Data

[7] We used broadband vertical component seismograms recorded by stations located in a latitudinal range from 20°S to 45°N and a longitudinal range from 110°E to 165°E: 18 F-net stations, 8 OHP stations, 4 IRIS stations, a station of the GEOSCOPE network, and 20 BBOBS stations. Locations, period of observations, network names, and sensors are listed in Table 1. Among the BBOBS stations, array stations across the northern Philippine Sea and in the Mariana trough were equipped with the PMD sensors manufactured by the PMD Scientific, Inc. Other stations in the northwestern Pacific Ocean, the Shikoku Basin, and the central Philippine Sea are equipped with the CMG-1T or CMG-3T sensors manufactured by the Guralp Systems Ltd. The PMD has a flat velocity response at periods from 0.05 to 30 s and the CMG-1T and CMG-3T sensors have a flat velocity response from 0.02 to 360 s. The seismograms recorded by the BBOBSs with the PMD sensors were corrected for their tilt of the sensors because the PMD sensor does not have an active leveling unit while the BBOBS with CMG-1T or CMG-3T has.

[8] We analyzed events which took place around the Philippine Sea since 1990. The body wave magnitudes are greater than 6.0 for land-based stations. To increase the number of the data observed by BBOBSs, we chose a smaller magnitude threshold of 5.5 for the BBOBS stations. Note that the observation period was less than one year for most of the BBOBS stations because of the temporal deployment, resulting in smaller amounts of data for the BBOBS stations than the land-based stations. The event and station locations are shown in Figure 1. We analyzed 1089 events, including 398 events with focal depths greater than 40 km.

3. The Three-Stage Inversion Method

[9] We employed the three-stage inversion method developed by *Yoshizawa and Kennett* [2004]. The method consists of three independent stages: (1) measurements of

Table 1. Locations and Observation Periods of the Broadband Stations Used in the Present Study

Station Code	Latitude	Longitude	Elevation	Period	System/Network	Sensor
NWPAC1	41.1180	159.9322	−5599	1999.08.20–2000.03.19	BBOBS	CMG-1T
NWPAC2	41.1185	159.9343	−5589	2000.05.28–2000.10.30	BBOBS	CMG-1T
NWPAC3	41.1291	159.9442	−5600	2001.07.31–2002.06.20	BBOBS	CMG-1T
NOT1	19.3423	135.1215	−5698	2002.03.25–2002.09.30	BBOBS	CMG-1T
SWSB1	25.7668	137.0118	−4915	2002.10.04–2003.05.09	BBOBS	CMG-3T
PHS03	13.479189	147.810356	−5570	1999.11.29–2000.07.16	BBOBS	PMD
PHS04	16.579678	144.696259	−3206	1999.11.29–2000.07.14	BBOBS	PMD
PHS05	17.787031	143.407408	−4083	1999.11.29–200.07.13	BBOBS	PMD
PHS08	21.407732	139.442632	−4911	1999.11.29–2000.07.11	BBOBS	PMD
PHS09	22.560394	138.121841	−5007	1999.11.29–2000.07.10	BBOBS	PMD
PHS11	25.000119	135.138480	−5340	1999.11.29–2000.05.12	BBOBS	PMD
PHS12	26.136514	133.676446	−5153	1999.11.29–2000.07.08	BBOBS	PMD
PHS13	27.188867	132.415377	−5428	1999.11.29–2000.07.07	BBOBS	PMD
MAR02	17.825050	143.543323	−5171	2001.10.08–2002.10.08	BBOBS	PMD
MAR04	18.131431	144.781421	−3478	2001.10.08–2002.09.16	BBOBS	PMD
MAR05	18.366010	145.750298	−2728	2001.10.08–2002.10.07	BBOBS	PMD
MAR06	18.550086	146.498567	−3698	2001.10.08–2002.09.28	BBOBS	PMD
MAR07	19.036187	148.435618	−5557	2001.10.08–2002.10.03	BBOBS	PMD
MAR08	17.899185	145.383667	−3509	2001.10.08–2002.09.24	BBOBS	PMD
MAR09	19.091788	145.380741	−3571	2001.10.08–2002.09.24	BBOBS	PMD
AMM	28.1534	129.3022	12	1999.03.20–	F-net	STS-1
HID	42.8183	142.4183	109	2000.12.29–	F-net	STS-2
HRO	37.2215	140.8813	630	2000.04.08–	F-net	STS-2
HSS	42.9647	141.2328	230	1996.09.14–	F-net	STS-1
IGK	24.4060	124.1783	77	2000.05.18–	F-net	STS-2
ISI	34.0572	134.4580	27	1996.03.09–	F-net	STS-1
JIZ	34.9129	138.9972	263	1995.03.17–	F-net	STS-1
KGM	26.7531	128.2168	102	2000.02.25–	F-net	STS-2
KIS	33.8627	135.8933	70	1999.03.07–	F-net	STS-1
KMU	42.2387	142.9670	185	1999.12.28–	F-net	STS-2
KSN	38.9733	141.5333	280	2000.02.11–	F-net	STS-2
NMR	43.3650	145.7420	20	1996.09.18–	F-net	STS-1
TKA	31.5125	130.7853	535	1996.03.15–	F-net	STS-1
TMR	41.0990	141.3868	120	1997.11.15–	F-net	STS-1
TSA	33.1744	132.8229	141	2000.03.10–	F-net	STS-2
TYM	34.9708	139.8481	30	1995.03.22–	F-net	STS-1
URH	42.9270	143.6746	75	1998.10.24–	F-net	STS-1
ZMM	26.2289	127.3058	22	2001.03.10–	F-net	STS-2
BAG	16.4108	120.5797	1507	1998.03.–	OHP	STS-1
ISG	24.3793	124.2347	27	1995.03.–	OHP	STS-1
JAY	−2.5147	140.7030	439	1997.12.–	OHP	STS-1
MCSJ	24.290	153.978	10	1996.12.–	OHP	STS-1
OGS	27.0570	142.2030	20	1992.07.–	OHP	STS-1
PALU	7.3436	134.4741	10	1996.04.–	OHP	STS-1
PATS	6.8367	158.3125	10	1995.06.–	OHP	STS-1
PMG	−9.41	141.16	?	1993.09.–	OHP	STS-1
GUMO	13.5878	144.8663	14(−100)	1991.07.08–	IRIS	KS-54000
TATO	24.9754	121.4881	−37	1992.09.26–	IRIS	KS-36000-i
MAJO	36.5425	138.2073	405(−48)	1990.08.20–	IRIS	STS-1
DAV	7.0878	125.5747	84(−1)	1994.12.18–	IRIS	STS-1
INU	35.350	137.029	132.3	1987.03.04–	GEOSCOPE	STS-1

multimode phase speed dispersion; (2) 2-D mapping of phase speed for each mode and period; and (3) inversion of multimode phase dispersion at each grid for 3-D shear wave speed model. We will explain the method step by step.

3.1. Measurement of Multimode Phase Speeds

[10] The first stage of the three-stage inversion is to measure multimode dispersion from observations. All seismograms are corrected for instrumental response, decimated to a sampling rate of 2 s and converted to displacements with a 5 mHz high-pass filter. We determined phase speeds of the fundamental and first three higher modes of Rayleigh waves from each seismogram by a fully nonlinear waveform inversion method [*Yoshizawa and Kennett*, 2002a]. In this inversion method, the neighborhood algorithm (NA) of *Sambridge* [1999] is adopted as a global optimizer that explores the model parameter space to find a model with the best fit to the data. The process to find the best model is as follows: (1) generate a path-averaged 1-D shear wave speed model using NA; (2) compute a synthetic waveform using this 1-D model; (3) calculate the misfit between the synthetic and observed waveforms; (4) repeat steps 1–3 until N (3000 in the present study) models are calculated; (5) find the best fitting 1-D model for which multimode phase dispersions are computed; and (6) estimate reliability of the dispersion measurement.

[11] For the computation of synthetic waveforms, the centroid moment tensor solutions reported by the Harvard University were used for source parameters in the present

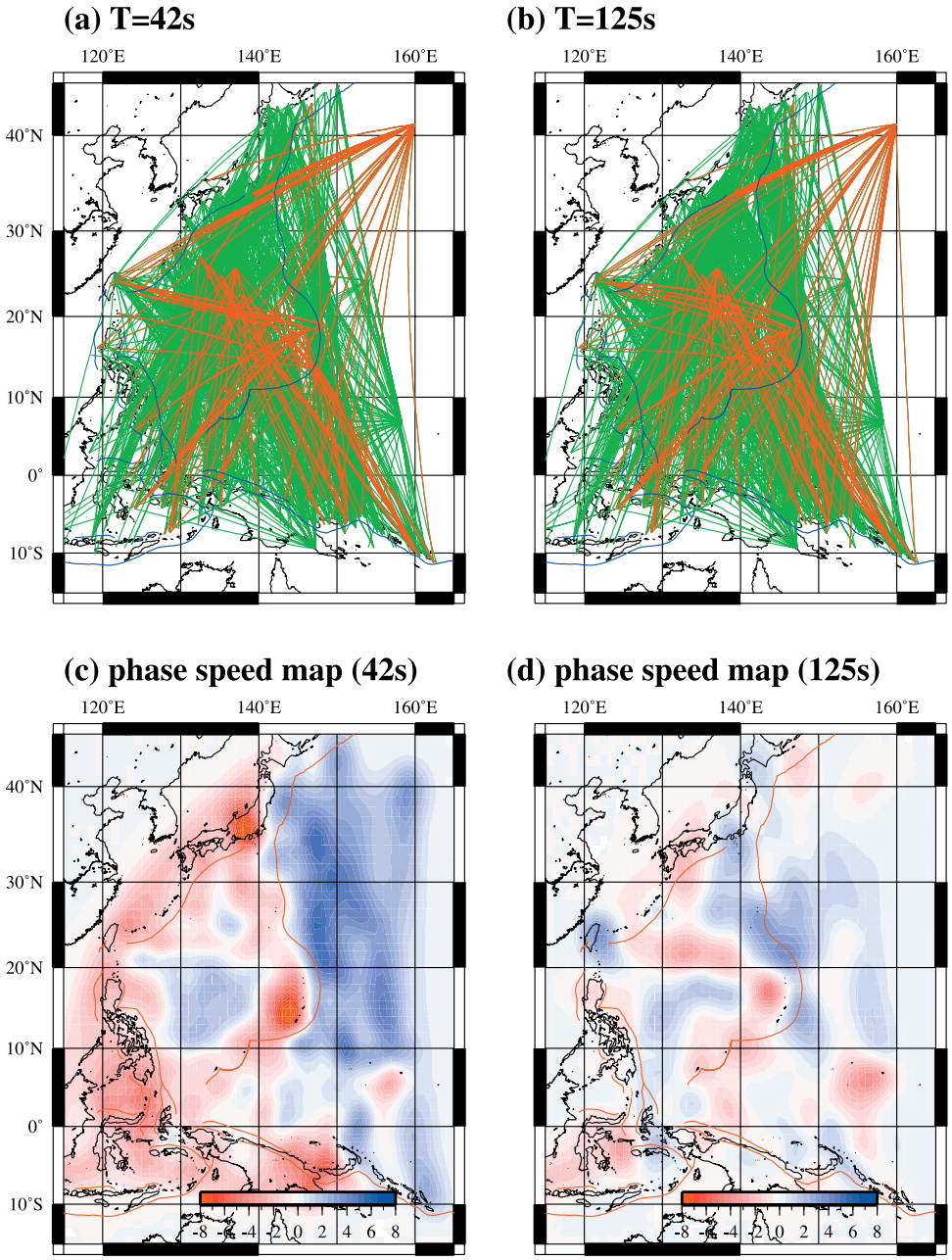

Figure 2. Ray path coverages at (a) 42 and (b) 125 s for the fundamental mode Rayleigh waves. All the rays are traced on the phase speed models at each period, taking the ray bending effect into account. The ray paths to the BBOBS stations are indicated in red. (c) and (d) The corresponding phase speed models, where the reference phase speeds are 3.93 and 4.16 km/s, respectively.

study. An initial shear wave speed model for island stations is based on PREM [*Dziewonski and Anderson*, 1981] with a crustal structure corrected with the 3SMAC model [*Nataf and Ricard*, 1996]. The same crustal correction is applied to a reference model for BBOBS stations, which is three percent slower than PREM from the Moho to 250 km depth to give a better fit to data. Three thousand models have been generated for each path, and the best fit 1-D model was obtained from the ensemble of models. We estimated the standard error of each dispersion curve from standard deviations of the best one thousand trials among all the generated models. The multimode phase speeds were then computed from the 1-D model using the normal mode theory [e.g., *Takeuchi and Saito*, 1972], which are regarded as the path-averaged phase speeds of each event-station pair. We took the reliability of phase speed measurement [*Yoshizawa and Kennett*, 2002a] to be greater than 4.5 and 2 for the fundamental and higher mode, respectively.

[12] We obtained 1087 phase speed dispersion curves for the fundamental mode Rayleigh wave at periods between 40 and 167 s, 82 for the first higher mode, 142 for the second higher mode and 95 for the third higher mode at periods between 40 and 120 s. Because of the shorter observation periods (Table 1), the number of dispersion curves obtained from BBOBS seismograms is

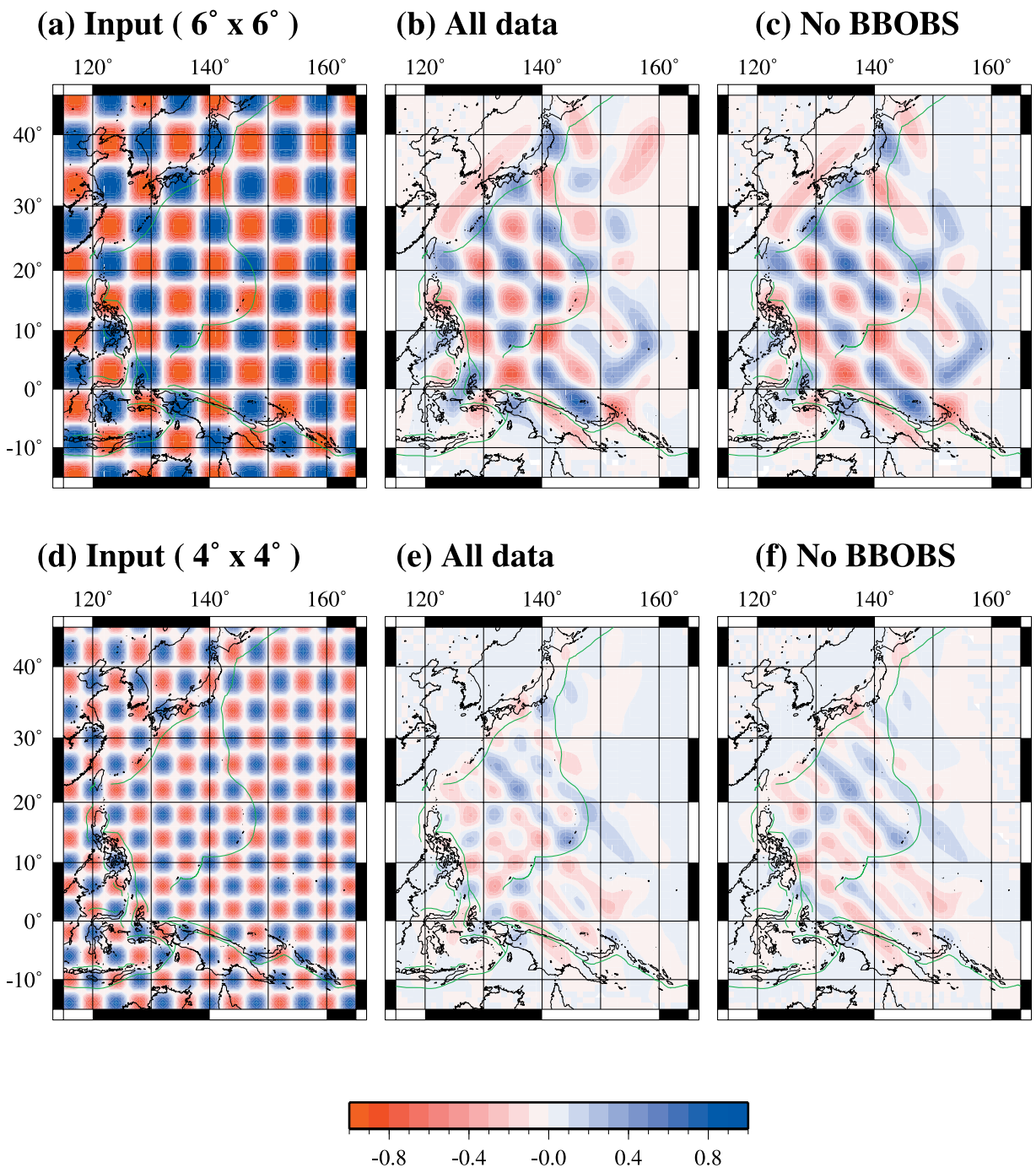

Figure 3. Checkerboard resolution test results for the fundamental mode with different cell sizes: (a–c) 6 × 6 degrees and (d–f) 4 × 4 degrees. From the left to right, the input checkerboard models (Figures 3a and 3d), the output models recovered from all the synthetic data (Figures 3b and 3e) and the output models recovered from those without BBOBS data (Figures 3c and 3f).

limited. 127, 6, 14, and 3 for the fundamental and the first three higher modes, respectively. The estimated errors for the fundamental mode are less than 0.02 km/s at periods shorter than 83 s and less than 0.03 km/s at the longer periods. Those for the higher modes are less than 0.04 km/s in the studied period range.

3.2. Inversion for 2-D Phase Speed Maps

[13] In the second stage, we invert the path-averaged multimode phase speeds to 2-D phase speed maps of each mode as a function of frequency. It is this stage to take into consideration the finite frequency effect and the ray path deviation from the great circle. The Fresnel area ray tracing technique [*Yoshizawa and Kennett*, 2002b] is used for tracing rays and calculating the width of the influence zone around the surface wave path at finite frequencies. *Yoshizawa and Kennett* [2002b] have identified with careful investigation of a stationary phase field that the influence zone of surface wave paths is nearly one third of the width

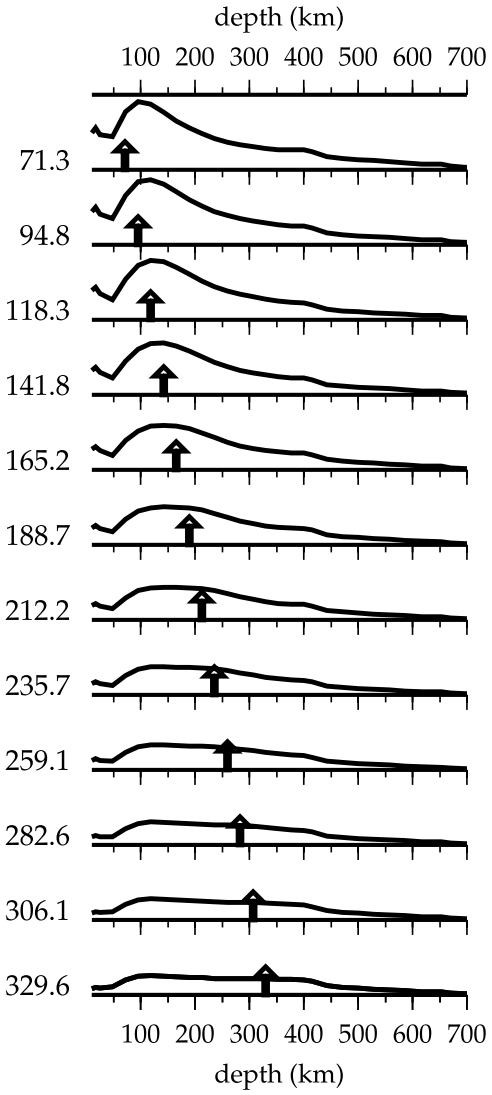

Figure 4. Resolution kernel of the 1-D shear wave speed profile for the site at 18°N and 144°E. The kernel should be delta-like at each depth shown by the arrow if the vertical resolution were perfect.

of the first Fresnel zone. Since the influence zone has been defined as the finite area over which surface waves are coherent in phase, we can regard the observed phase speed as an average within the influence zone rather than just as an average along the path.

[14] Using the ray centered coordinate system (s,n), where s is a length along a path and n is an off distance from the path, the linear relation for average phase speed along the ray can be represented as follows:

$$\left\langle \frac{\delta c}{c_0} \right\rangle_{\text{path}} = \frac{1}{\Delta} \int_{\text{path}} ds \frac{1}{2N_w(s)} \int_{\text{width}} dn W(s,n) \frac{\delta c(s,n)}{c_0}, \qquad (1)$$

where c is phase speed and $N_w(s) = \int dn W(s,n)$ is understood as the effective width of the influence zone. We adopt a cosine taper as the weight function $W(s,n)$ over the width of the influence zone to smooth the edges of the influence zone at which the assumption of the phase coherency tends to be violated [*Yoshizawa and Kennett*, 2004]:

$$W(s,n) = \cos\left[\frac{\pi}{2}\left(\frac{n}{N(s)}\right)^2\right].$$

The integration along the path should be undertaken between the two edges of the influence zone. The length of the influence zone should be slightly longer than the ray path length by one sixth of the wavelength, since the zone is not confined between the source and receiver, which extends slightly behind the source and receiver locations as shown by *Yoshizawa and Kennett* [2002b].

[15] The influence zone becomes wider at longer periods because the absolute phase speed is faster. From (1) we can obtain an expression of the two-dimensional distribution of sensitivity to surface wave phase. The weighted surface wave sensitivity to phase speed structure varies along the path but is nearly constant over the width of influence zone and highest sensitivity is concentrated near the source and receiver [see, e.g., *Yoshizawa and Kennett*, 2004, Figure 4].

[16] Equation (1) can be written as a generalized form, $\mathbf{d} = \mathbf{Gm}$, where the data vector $\mathbf{d}$ consists of the observed phase speed variations $\langle \delta c/c_0 \rangle_i (i = 1, 2, .., M)$ and M is the total number of paths; $\mathbf{m}$ is a vector of model parameters m_j ($j = 1, 2, .., N$) and N is the total number of model parameter and $\mathbf{G}$ is the kernel matrix. In the present study, we use a spherical B spline function $F(\theta, \phi)$ defined at the center of a geographic cell as a basis function [e.g., *Lancaster and Salkauskas*, 1986; *Wang and Dahlen*, 1995] to expand the phase speed perturbation:

$$\frac{\delta c(\theta,\phi)}{c_0} = \sum_{j=1}^{N} m_j F_j(\theta,\phi),$$

where the model parameter m_j is the coefficient of the jth basis function F_j.

[17] Using the B spline function, the components of the kernel matrix $\mathbf{G}$ can be written as follows:

$$G_{ij} = \frac{1}{\Delta_i} \int_0^{\Delta i} ds F_j,$$

when we ignore the finite frequency effect, and

$$G_{ij} = \frac{1}{\Delta_i} \int_0^{\Delta_i} ds \frac{1}{2N_w(s)} \int_{\text{width}} dn W(s,n) F_j,$$

when we take the finite frequency effect into account using the influence zone. The ray paths have been computed using a technique of Fresnel area ray tracing [*Yoshizawa and Kennett*, 2002b]. The epicentral distance Δ_i is measured along the ray path.

[18] We solved the linearized inversion equation with a damped least squares scheme, minimizing the objective function

$$\Phi(\mathbf{m}) = (\mathbf{d} - \mathbf{Gm})^T \mathbf{C}_d^{-1} (\mathbf{d} - \mathbf{Gm}) + \lambda^2 \mathbf{m}^T \mathbf{m}, \qquad (2)$$

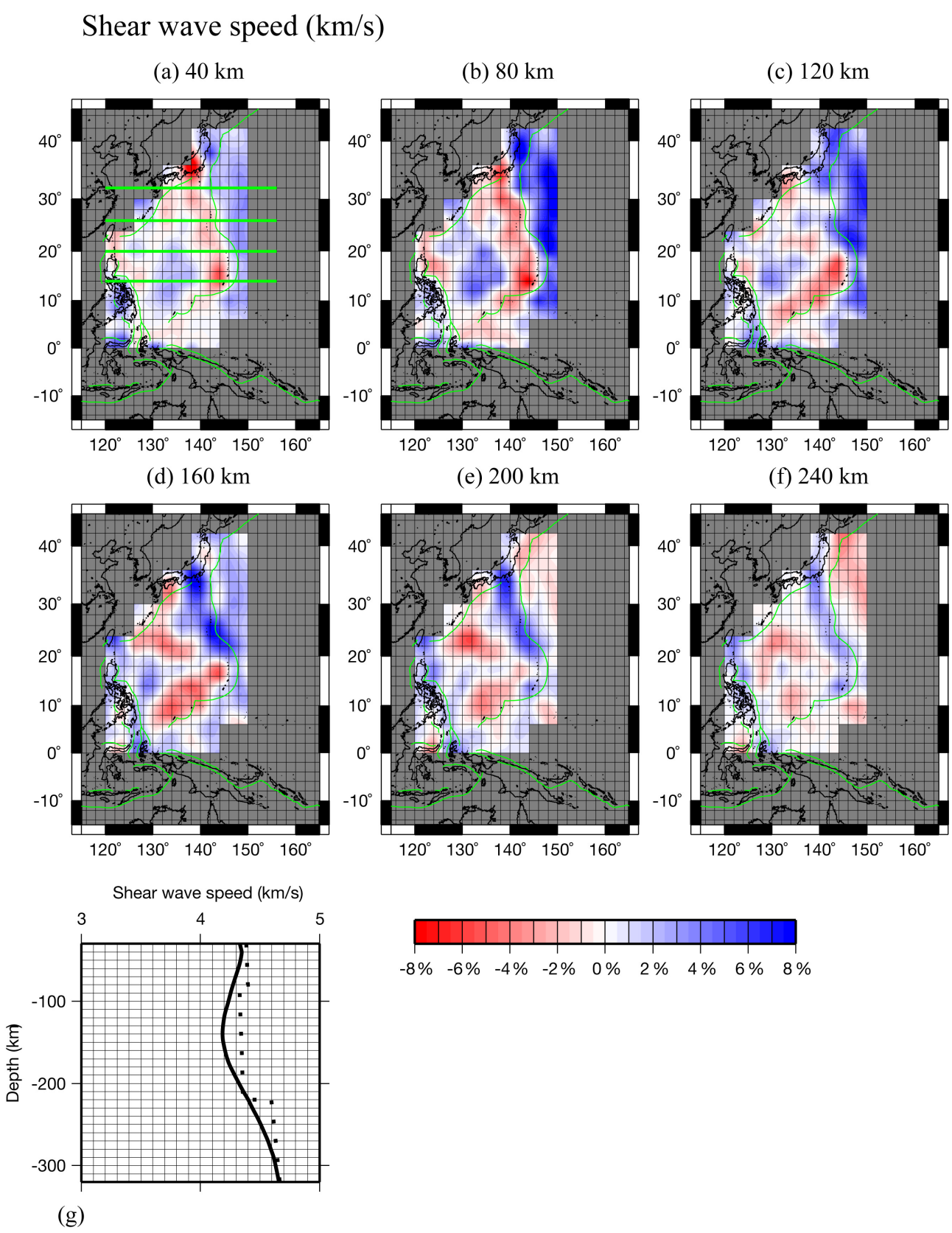

Figure 5. Map projections of the shear wave speed at depths (a) 40, (b) 80, (c) 120, (d) 160, (e) 200, and (f) 240 km. (g) The reference shear wave speed profile (solid line), which is the laterally averaged structure of our 3-D model. The dashed line in Figure 5g is the SV wave speed of PREM at a reference period of 100 s. Green solid lines in Figure 5a show the location of the cross sections given in Figure 6.

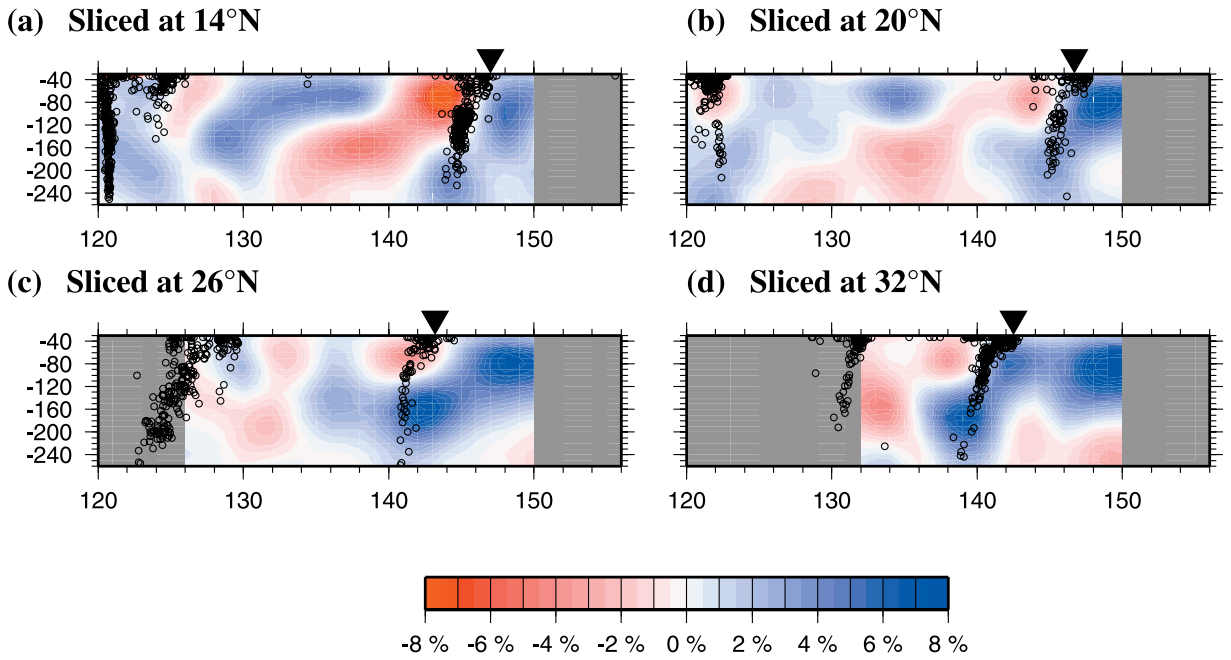

Figure 6. Cross sections of our 3-D shear wave speed model. See Figure 5a for the locations of these cross sections. The subducted Pacific slab can be seen clearly. Inverted triangle on the top of each panel shows the location of the axis of Izu-Bonin-Mariana trench.

where C_d^{-1} is the inverse data covariance matrix and λ is an arbitrary damping parameter that controls the trade-off between the model variance and resolution. Assuming that measured phase speeds for different paths are uncorrelated and their variances are mutually different, the covariance matrix can be represented as $\mathbf{C}_d = \sigma_{d_i}{}^{-1}\mathbf{I}$, where σ_{d_i} is the measurement error for the ith datum.

[19] The equation (2) can be represented as $\Phi(\mathbf{m}') = |\mathbf{d}' - \mathbf{G}'\mathbf{m}|^2 + \lambda^2|\mathbf{m}|^2$, where $d_i' = d_i/\sigma_{d_i}$ and $G_{ij}' = G_{ij}/\sigma_{d_i}$.

[20] The inverse problem is then to solve the linear equation system

$$\begin{bmatrix} \mathbf{G}' \\ \lambda\mathbf{I} \end{bmatrix} \mathbf{m} = \begin{bmatrix} \mathbf{d}' \\ \mathbf{0} \end{bmatrix},$$

for which we use the iterative LSQR algorithm [*Paige and Saunders*, 1982].

3.2.1. Multimode Phase Speed Map

[21] By the method described above we inverted the path-averaged phase dispersion curves obtained in the first stage for the 2-D multimode phase speed maps with a grid interval of 2.0° at periods between 39 and 167 s for the fundamental mode, between 39 and 125 s for the first and second higher modes, and between 39 and 83 s for the third higher mode. The phase speed maps obtained at the initial iteration are those corrected for the finite frequency effect via the influence zone around the great circle paths. Then we use these maps as laterally heterogeneous reference models to incorporate the effects of ray bending as well as the effects of finite frequency around the ray path for updating the phase speed models.

[22] Considering a trade-off between misfits of data and variance of parameters, we chose $\lambda = 1.5$ as the damping parameter for the fundamental mode and $\lambda = 0.7$ for the higher modes in the present study. The variance reductions for the fundamental mode are about 80, 48 and 33% at periods of 42,125 and 167 s, respectively. The variance reductions of first higher mode are about 58 and 68%, those of second higher mode are about 52 and 73% and those of third higher mode are about 48 and 68% at periods of 42 and 125 s. Figures 2a and 2b show the path coverage for the fundamental mode at periods of 42 and 125 s which were calculated from the final 2-D phase speed maps shown in Figures 2c and 2d, respectively. The rays well cover the Philippine Sea and the westernmost Pacific Ocean near the Izu-Bonin-Mariana trench.

[23] The final 2-D phase speed maps at 42 and 125 s are shown in Figures 2c and 2d. There are slow phase speed anomalies along the Izu-Bonin-Mariana trench, fast phase speed anomalies in the West Philippine Basin and the Pacific Ocean at a period of 42 s. The fast phase speed anomalies exist along the Izu-Bonin-Mariana trench at a period of 125 s. The slow phase speed anomalies exist at the Mariana trough at periods of 42 and 125 s.

3.2.2. Checkerboard Resolution Test

[24] To see how these maps could be distorted by nonuniform path coverage, we performed checkerboard resolution test with different cell sizes: 6 degrees (Figures 3a–3c) and 4 degrees (Figures 3d–3f) at a period of 42 s. In this resolution test, we have used the ray paths shown in Figure 2a which we have calculated with the effect of ray bending and finite frequency. In case of the 6-degree cell, checkerboard patterns and amplitude are well retrieved in the Philippine Sea region including the Izu-Bonin-Mariana trench, whereas, for the 4-degree case, the patterns are well recovered in the same region but the amplitude decreases to be a half of the input checkerboard (Figures 3b and 3e). In the Pacific region, the recovery of the patterns of 4-degree

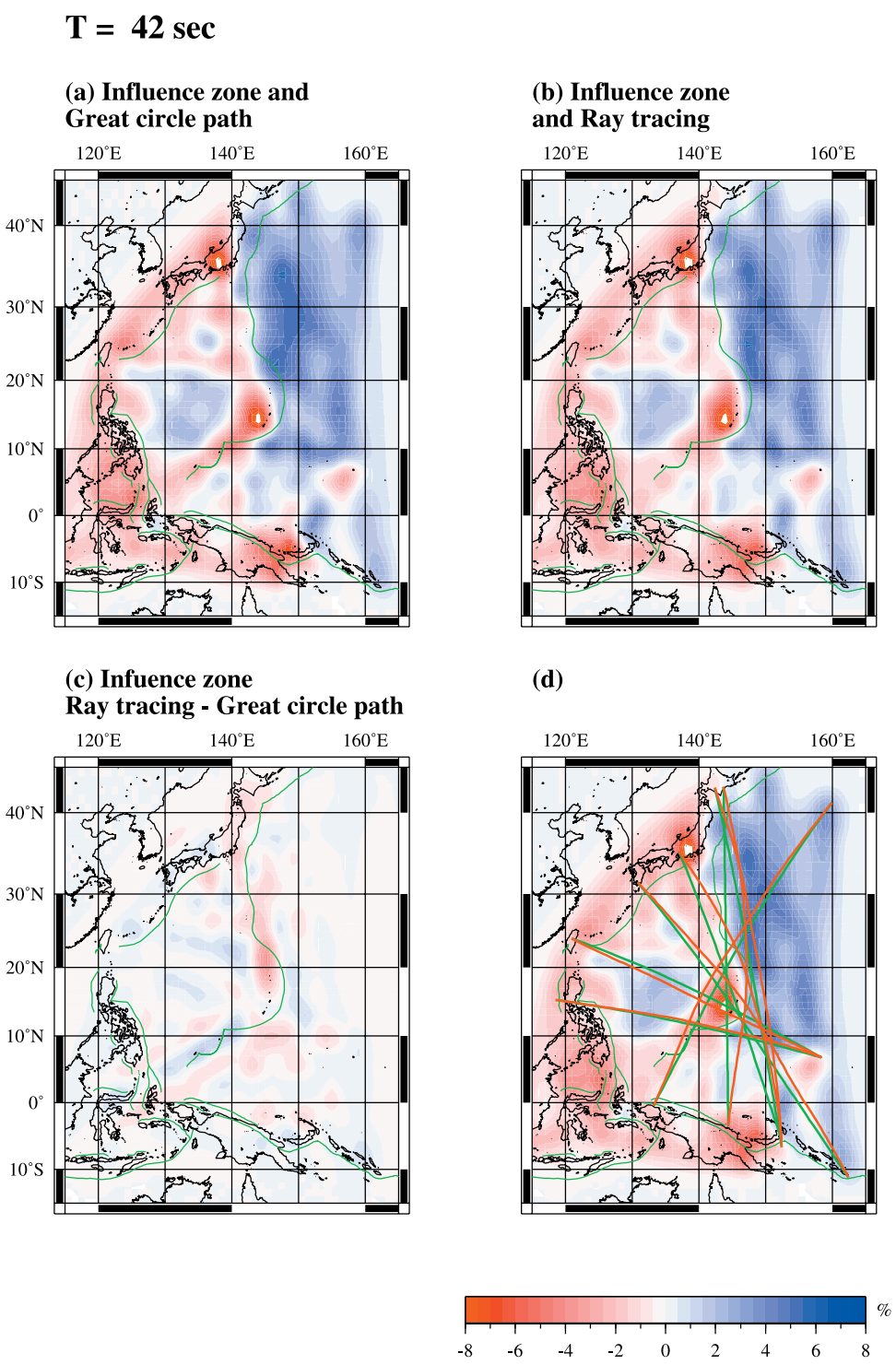

Figure 7. Map projections of the fundamental mode phase speed at a period of 42 s taking into account of the effect of finite frequency via the influence zone around the great circle paths. The effect of ray bending is (a) not taken into account and (b) taken into account. (c) Difference in phase speed between the two models. (d) Examples of the off-great circle paths (red solid lines) and their great circle paths (green thick solid lines). The phase speed map in Figure 7d is the same of that in Figure 7b.

cell is not satisfactory, while the patterns of 6-degree cell are well retrieved in the region to the west of 150°E. The heterogeneity patterns are elongated in the northwest-southeast direction in the Caroline sea, where a majority of surface waves used in the present study are traveling in such directions.

[25] Though the checkerboard patterns in the northern Philippine sea region are somewhat elongated, each cell shape can be clearly identified and thus the phase speed

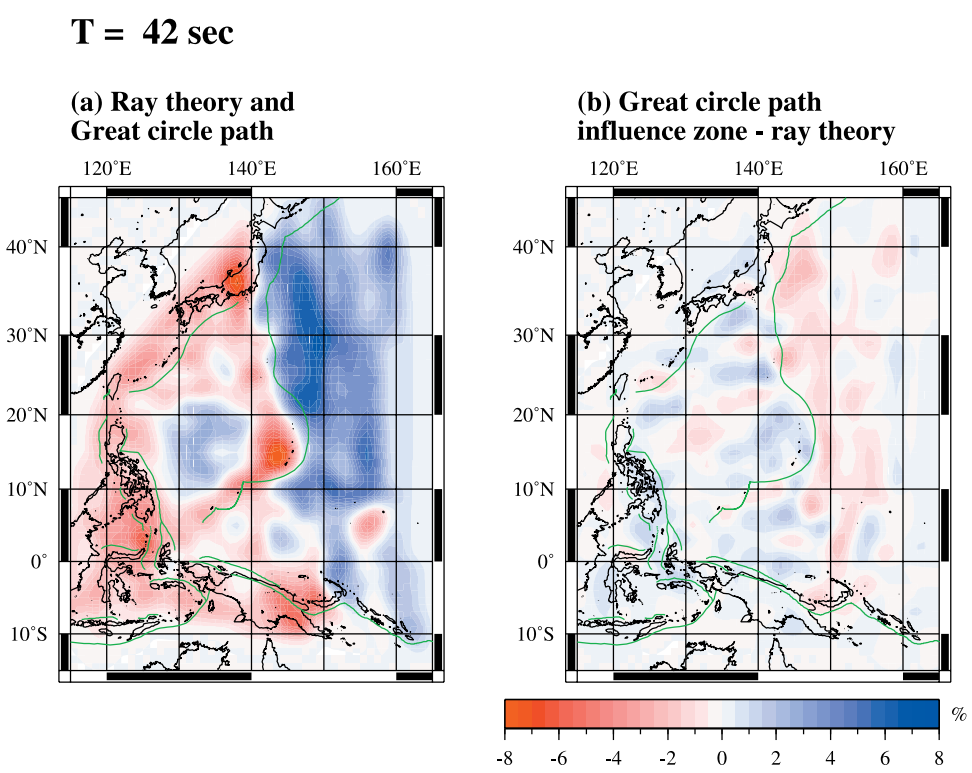

Figure 8. (a) Map projection of the fundamental mode phase speed at a period of 42 s obtained by ray theory with the great circle approximation. (b) Difference in phase speed between the model with the influence zone (Figure 7a) and the model with ray theory Figure 8a.

maps are not severely distorted by the 2-D tomographic process in the Philippine sea region. The spatial resolution is estimated to be about 300 km in better resolved regions of the Philippine Sea and about 400 km on the average. The resolution is poorer on the Pacific Ocean side.

3.2.3. Improvement of the Result by Using BBOBS Seismograms

[26] Figures 2a and 2b shows the ray coverage using land-based and BBOBS seismograms. These indicate that the use of BBOBS data has improved the ray coverage in the southern Philippine Sea region and the northwestern Pacific Ocean. Figures 3c and 3f display the results of checkerboard resolution tests with no BBOBS data. We used only land-based seismograms for the results in Figures 3c and 3f. Figures 3c and 3f shows that the shapes of 4-degree and 6-degree cells are elongated in the northwest-southeast direction in the Philippine Sea region and are not retrieved in the Pacific Ocean. These suggest that the horizontal resolution in the previous studies based only on land-based seismograms is likely to be more degraded than in the present study.

[27] Even though the number of BBOBS data is only about 10% in our data set, the BBOBS data contribute to our result significantly and are of great help in improving our tomographic model.

3.3. Inversion for 3-D Shear Speed Model

[28] The third stage of the three-stage inversion method is to invert the multimode dispersion curves obtained at each grid of phase speed maps for the shear wave speed model in that grid. The multimode phase dispersion can be represented as a function of density, P wave speed, and shear wave speed. We fixed the density and P wave speed structure to the reference model and solved only for shear wave speed, since the effects of density and P wave speed on Rayleigh wave phase speed perturbation are not significant [*Nataf et al.*, 1986]. The iterative least squares inversion by *Tarantola and Valette* [1982] is used for the inversion.

[29] In this inversion, the degree of the perturbation and the smoothness of the depth variation are controlled via a priori model covariance with a Gaussian distribution. We have used a standard deviation σ = 0.1 km/s and a correlation length L = 5 km above the Moho, L = 10 km from the Moho to 60 km depth and L = 20 km below 60 km depth so that large perturbations are allowed in the crust. The reference 1-D model is based on PREM except for the crust for which we adopted the CRUST2.0 model [*Bassin et al.*, 2000].

4. The 3-D Shear Wave Speed Model Beneath the Philippine Sea

[30] Figure 4 shows the resolution kernel of the typical 1-D shear wave speed profile at 18°N and 144°E, suggesting sufficient resolution down to a depth of 250 km beneath the Philippine Sea.

[31] Figures 5a–5f show the geographical distributions of the inverted 3-D shear wave speed beneath the Philippine Sea. We show only well resolved area. The shallowest 100 km of the upper mantle is slow in the Izu-Bonin-Mariana back arc and fast beneath the West Philippine

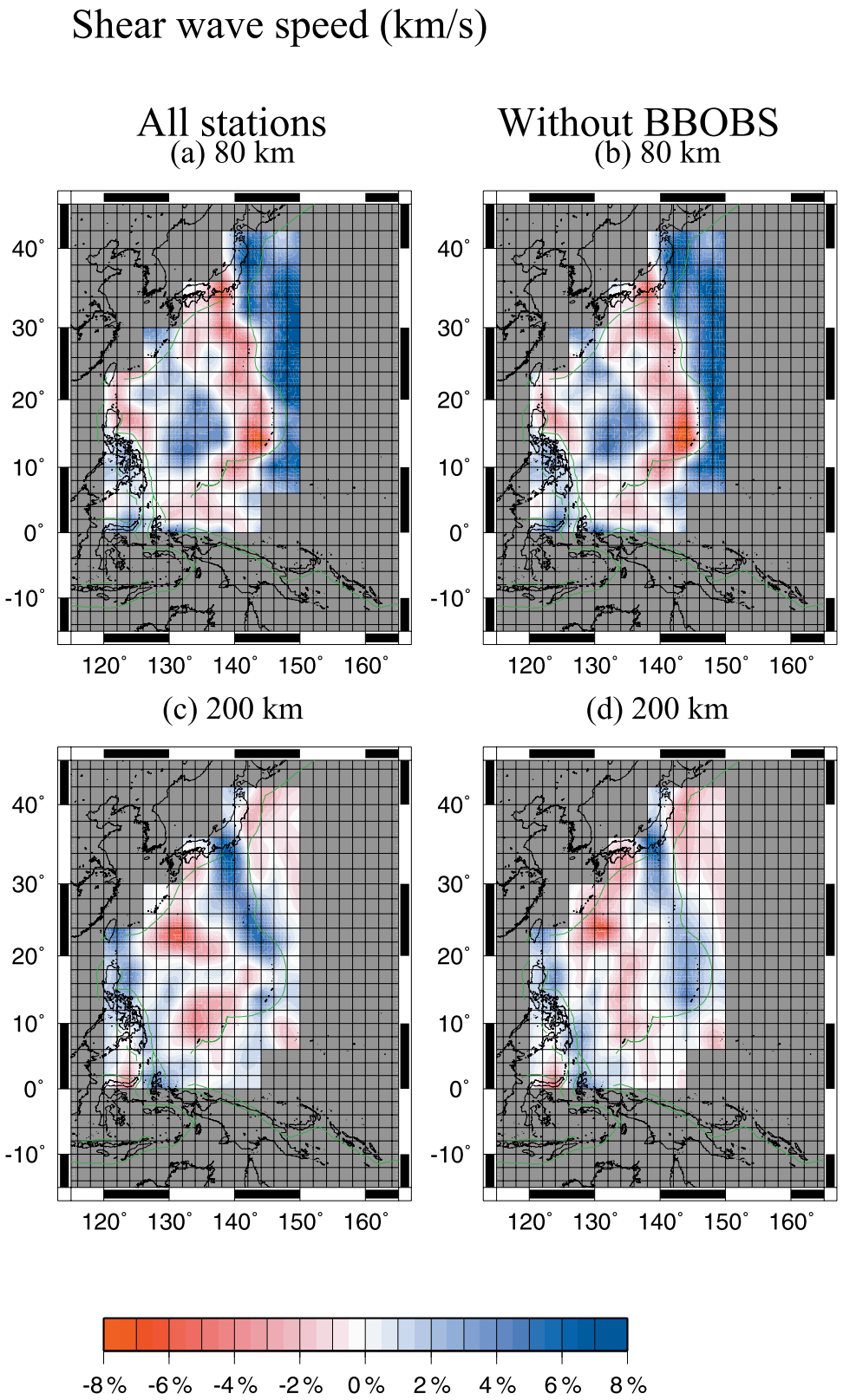

Figure 9. Comparison of the shear wave speed models with and without the BBOBS data. The shear wave speed maps at depths of (a and b) 80 km and (c and d) 200 km are shown. The BBOBS data are used in Figures 9a and 9c and not used in Figures 9b and 9d.

Basin. There is a striking wave speed contrast across the Izu-Bonin-Mariana trench, where the mantle on the Pacific side is about 6% faster than the mantle on the Philippine Sea side down to 120 km depth. Figure 5g shows the depth profile of the average shear wave speed of the upper mantle beneath the Philippine Sea, indicating a significantly slower upper mantle on the whole than PREM.

[32] The speed is lowest under the Mariana trough where the low-speed anomalies reach 10% and continue down at least to 200 km. The mantle under the Daito ridge and the Shikoku Basin is slightly slow down to 80 km depth, where the inverted speed may be in part affected by the thick crust reported beneath the Daito ridge [*Nishizawa et al.*, 1983, 2004]. The pattern of lateral variation changes across depths from 120 to 160 km.

[33] In the upper 120 km, the shear wave speed structure is well correlated with the age of the provinces: the wave speed is fastest beneath the oldest region (150 Ma for the Pacific Ocean) and decreases as the age of the province becomes younger (33–49 Ma for the West Philippine Basin; 15–27 Ma for the Parece-Vela Basin; 0–6 Ma for the Mariana trough). This suggests that the relatively high wave speed portion in the uppermost mantle corresponds to the oceanic lithosphere, which is thicker in the older region than in the younger region, although it is difficult to define the thickness quantitatively in the present study because of our parameterization allowing for continuous shear wave speed variation. The above correlation is qualitatively consistent with the previous studies showing thick lithospheres beneath the Pacific Ocean and the West Philippine Basin and a thin lithosphere beneath the eastern Philippine Sea [e.g., *Shiono et al.*, 1980; *Oda and Senna*, 1994].

[34] At depths greater than 160 km, the anomaly pattern is dominated by fast anomalies of the subducted Pacific slabs and slow anomalies uncorrelated with the surface tectonics as shown in Figures 5d–5f. The fast anomalies along the Izu-Bonin arc are shifted westward with depth, delineating the subducted Pacific slab dipping to the west. The westward dipping slab anomaly is a persistent feature along the Izu-Bonin-Mariana arc, as shown in the cross sections in Figure 6.

[35] Figure 5 shows the slow anomaly at depths greater than 160 km to the south of the Daito ridge. This slow anomaly trends in the NW-SE direction apparently in parallel with the Daito ridge. Another deep slow anomaly is seen at depth greater than 160 km under the southern part of the Philippine Sea.

5. Discussions

[36] Figure 7 demonstrates the effect of ray bending for the fundamental Rayleigh wave at a period of 42 s. Figures 7a and 7b show the perturbation maps obtained by ignoring and allowing for the effect of ray bending, respectively, and in Figure 7c we take their difference. The large-scale structures, such as fast anomalies in the Pacific Ocean, slow anomalies along the eastern periphery of the Philippine Sea, are similar in both models. However, the detail of the transition from the fast to slow anomalies is different between the two models, particularly in the northern part of the Mariana Islands around at 20°N, where the phase speed difference exceeds 2–4%, as indicated in Figure 7c. For the model with ray bending, the region with slow phase speed anomalies is more closely adjacent to the Izu-Bonin-Mariana trench. For the model without the bending effect, on the other hand, the transition from the slow to fast anomalies does not occur exactly along the trench: the fast anomalies on the oceanic side continue further westward to the inner side across the trench. This westward leakage of the fast anomaly is likely to be an artifact due to ignoring the effect of ray bending. Figure 7d shows that the actual ray paths depart from their great circle path, especially when they graze the Izu-Bonin-Mariana trench zone. The off-great circle path effect is not significant for rays passing mostly through the Pacific Ocean or the Philippine Sea. It is important to consider the effect of ray bending, especially in regions involving sharp speed change such as the trench or the ocean-continent boundary.

[37] Figure 8 demonstrates the effect of finite frequency of the fundamental Rayleigh wave at a period of 42 s. Figure 8a shows the perturbation map obtained by the ray theory with the great circle approximation. Figure 8b displays a differential map between the ray theoretical model (Figure 8a) and the finite frequency model (Figure 7a) with the effects of the influence zone around the great circle path. Heterogeneity in both models are similar and the phase speed differences of models are less than 1.5% in most areas (Figures 7a, 8a, and 8b). In the Pacific Ocean, phase speeds of the models with ray theory are faster than those of the models with the influence zone. In the Philippine Sea, we are able to find no systematic difference. *Yoshizawa and Kennett* [2004] have demonstrated that the recovery of heterogeneity patterns and amplitude can be improved with the influence zone, resulting in a better resolution and accuracy of the finite frequency models. Thus we have taken into account of the influence zone in our final model in Figure 5.

[38] To examine the improvement by the seafloor data, we compared the models obtained with and without the BBOBS data in Figure 9. At a depth of 80 km, the differences between the two models are not so large, but the model with the BBOBS data shows stronger slow anomalies on the back-arc side of the Izu-Bonin trench and more laterally variable fast anomalies on the Pacific side of the Izu-Bonin-Mariana trench. At a depth of 200 km, there are obvious differences between the two models (Figures 9c and 9d): The model with the BBOBS data shows slow anomalies in the Mariana trough while the model without the BBOBS data does not. The subducted Pacific slab is more clearly imaged in the model with the BBOBS data than without them. We believe that the present model has higher spatial resolution and accuracy over the previous models [*Nakamura and Shibutani*, 1998; *Lebedev et al.*, 1997; *Lebedev and Nolet*, 2003], since the ray bending effect, as well as the finite frequency effect, was taken into consideration and since the BBOBS data were used. We plan to deploy another BBOBS array from 2005 for 4 years, which will enable us to determine more detailed structure under the Philippine Sea and to study the evolution of the Philippine sea region.

[39] **Acknowledgments.** We thank staffs of IRIS, GEOSCOPE, OHP, and F-net data center for their effort to maintain and manage the seismic stations. We also thank two anonymous reviewers and an Associate Editor

for their helpful comments. This work was supported by Grant-in-Aid for Scientific Research [KAKENNHI, 15740282,15740266] from Japan Society for the Promotion Science. The GMT software package [*Wessel and Smith*, 1991] and SAC2000 [*Goldstein and Minner*, 1996] were used in this study.

References

Bassin, C., G. Laske, and G. Masters (2000), The current limits of resolution for surface wave tomography in North America, *Eos Trans AGU*, *81*(48), Fall Meet. Suppl., Abstract S12A-03.

Dziewonski, A. M., and D. L. Anderson (1981), Preliminary reference Earth model, *Phys. Earth Planet. Inter.*, *25*, 297–356.

Fukao, Y., Y. Morita, M. Shinohara, T. Kanazawa, H. Utada, H. Toh, T. Kato, T. Sato, H. Shiobara, N. Seama, H. Fujimoto, and N. Takeuchi (2001), The Ocean Hemisphere Network Project (OHP), in *Workshop Report of OHP/ION Joint Symposium, Long-Term Observations in the Oceans*, edited by B. Romanowicz, K. Suyehiro, and H. Kawakatsu, pp. 13–29, Earthquake Res. Inst., Univ. of Tokyo, Tokyo.

Fukuyama, E., M. Ishida, S. Hori, S. Sekiguchi, and S. Watada (1996), Broadband seismic observation conducted under the FREESIA project (in Japanese with English abstract), *Rep. Natl. Res. Inst. Earth Sci. Disaster Prevent.*, *57*, 23–31.

Goldstein, P., and L. Minner (1996), SAC2000: Seismic signal processing and analysis tools for the 21st century, *Seismol. Res. Lett.*, *67*, 39.

Hall, R., J. R. Ali, C. D. Anderson, and S. J. Baker (1995), Origin and motion history of the Philippine sea plate, *Tectonophysics*, *251*, 229–250.

Hussong, D. M., and S. Uyeda (1981), Tectonic processes and the history of the Mariana arc: A synthesis of the results of Deep Sea Drilling Project Leg 60, *Initial Rep. Deep Sea Drill. Proj.*, *60*, 909–929.

Isse, T., H. Shiobara, Y. Fukao, K. Mochizuki, T. Kanazawa, H. Sugioka, S. Kodaira, R. Hino, and D. Suetsugu (2004), Rayleigh wave phase velocity measurements across the Philippine Sea from a broadband OBS array, *Geophys. J. Int.*, *158*, 257–266, doi:10.1111/j.1365-246X.2004.02322.x.

Kanamori, H., and K. Abe (1968), Deep structure of island arcs as revealed by surface waves, *Bull. Earthquake Res. Inst. Univ. Tokyo*, *46*, 1001–1025.

Kanazawa, T., H. Shiobara, M. Mochizuki, M. Shonohara, and E. Araki (2001), Seismic observation system on the sea floor, in *Proceedings of OHP/ION Joint Symposium, Long-Term Observations in the Oceans*, edited by B. Romanowicz, K. Suyehiro, and H. Kawakatsu, Abstract S11–06, Earthquake Res. Inst., Univ. of Tokyo, Tokyo.

Kato, M., and T. H. Jordan (1999), Seismic structure of the upper mantle beneath the western Philippine Sea, *Phys. Earth Planet. Inter.*, *110*, 263–283.

Kennett, B. L. N., and K. Yoshizawa (2002), A reappraisal of regional surface wave tomography, *Geophys. J. Int.*, *150*, 37–44.

Lancaster, P., and K. Salkauskas (1986), *Curve and Surface Fitting*, Elsevier, New York.

Lebedev, S., and G. Nolet (2003), Upper mantle beneath Southeast Asia from *S* velocity tomography, *J. Geophys. Res.*, *108*(B1), 2048, doi:10.1029/2000JB000073.

Lebedev, S., G. Nolet, and R. D. van der Hilst (1997), The upper mantle beneath the Philippine Sea region from waveform inversions, *Geophys. Res. Lett.*, *25*, 1851–1854.

Nakamura, Y., and T. Shibutani (1998), Three-dimensional shear velocity structure in the upper mantle beneath the Philippine Sea region, *Earth Planets Space*, *50*, 939–952.

Nataf, H. C., and T. Ricard (1996), 3SMAC: An a priori tomographic model of the upper mantle based on geophysical modeling, *Phys. Earth Planet. Inter.*, *95*, 101–122.

Nataf, H. C., I. Nakanishi, and D. L. Anderson (1986), Measurements of mantle wave velocities and inversion for lateral heterogeneities and anisotropy: 3. inversion, *J. Geophys. Res.*, *91*(B7), 7261–7307.

Nishizawa, A., K. Suyehiro, and H. Shimizu (1983), Seismic refraction experiment at the Amami Plateau, *J. Phys. Earth*, *31*, 159–171.

Nishizawa, A., Y. Kaneda, Y. Katagiri, T. Morishita, J. Kasahara, S. Uno, Y. Nakajima, R. Kubota, and E. Nishiyama (2004), Crustal structure around the Oki-Daito Ridge in the northern West Philippine Basin, paper presented the 2004 Fall Meeting, Seismol. Soc. of Jpn., Fukuoka, Japan.

Oda, H., and N. Senna (1994), Regional variation in surface wave group velocitiesin the Philippine Sea, *Tectonophysics*, *233*, 265–277.

Okino, K., Y. Ohara, S. Kasuga, and Y. Kato (1999), The Philippine Sea: New survey results reveal the structure and the history of the marginal basins, *Geophys. Res. Lett.*, *26*, 2287–2290.

Paige, C. C., and M. A. Saunders (1982), LSQR: An algorithm for sparse linear equations and sparse least squares, *Trans. Math. Software*, *8*, 43–71.

Sambridge, M. (1999), Geophysical inversion with a neighbourhood algorithm-I. Searching a parameter space, *Geophys. J. Int.*, *138*, 479–494.

Seekins, L. C., and T. Teng (1977), Lateral variations in the structure of the Philippine Sea plate, *J. Geophys. Res.*, *82*, 317–324.

Shiobara, H., M. Kato, H. Sugioka, S. Yoneshima, K. Mochizuki, M. Mochizuki, S. Kodaira, R. Hino, M. Shinohara, and T. Kanazawa (2001), Long term observation by ocean bottom seismometer array on trans-PHS profile, in *Proceedings of OHP/ION Joint Symposium, Long-Term Observations in the Oceans*, edited by B. Romanowicz, K. Suyehiro, and H. Kawakatsu, Abstract S11–10, Earthquake Res. Inst., Univ. of Tokyo, Tokyo.

Shiono, K., I. S. Sacks, and A. T. Linde (1980), Preliminary velocity structure of Japanese Islands and Philippine Sea from surface wave dispersion, *Year Book Carnegie Inst. Washington*, *79*, 498–505.

Takeuchi, H., and M. Saito (1972), Seismic surface waves, in *Seismology: Surface Waves and Free Oscillations*, *Methods Comput. Phys.*, vol. 11, edited by B. A. Bolt, pp. 217–295, Elsevier, New York.

Tarantola, A., and B. Valette (1982), Generalized nonlinear inverse problems solved using the least-squares criterion, *Rev. Geophys.*, *20*, 219–232.

Taylor, B., and A. M. Goodliffe (2004), The West Philippine Basin and the initiation of subduction, revisited, *Geophys. Res. Lett.*, *31*, L12602, doi:10.1029/2004GL020136.

Wang, Z., and F. A. Dahlen (1995), Spherical-spline parameterization of three-dimensional Earth models, *Geophys. Res. Lett.*, *22*, 3099–3102.

Wessel, P., and W. H. F. Smith (1991), Free software helps map and display data, *Eos Trans. AGU*, *72*, 441, 445–446.

Yoshizawa, K., and B. L. N. Kennett (2002a), Non-linear waveform inversion for surface waves with a neighbourhood algorithm: Application to multimode dispersion measurements, *Geophys. J. Int.*, *149*, 118–133.

Yoshizawa, K., and B. L. N. Kennett (2002b), Determination of the influence zone for surface wave paths, *Geophys. J. Int.*, *149*, 440–453.

Yoshizawa, K., and B. L. N. Kennett (2004), Multimode surface wave tomography for the Australian region using a three-stage approach incorporating finite frequency effects, *J. Geophys. Res.*, *109*, B02310, doi:10.1029/2002JB002254.

Y. Fukao, T. Isse, H. Shiobara, D. Suetsugu, and H. Sugioka, Institute for Research on Earth Evolution, JAMSTEC, 2-15, Natsushima-cho,Yokosuka, Kanagawa, 237-0061, Japan. (isse@jamstec.go.jp)

T. Kanazawa, K. Mochizuki, K. Nakahigashi, S. Oki, and M. Shinohara, Earthquake Research Institute, University of Tokyo, 1-1-1, Yayoi, Bunkyo-ku, Tokyo, 113-0032 Japan.

K. Suyehiro, JAMSTEC, 2-15, Natsushima-cho, Yokosuka, Kanagawa, 237-0061, Japan.

K. Yoshizawa, Division of Earth and Planetary Sciences, Hokkaido University, Sapporo, 060-0810, Japan.